Prediction of Divertor Heat Flux Width for ITER Using BOUT++ Transport and Turbulence Module

Ze-Yu Li[1,2], Xue-Qiao Xu[2,1], Na-Mi Li[3,2], V S Chan[4,5], Xiao-Gang Wang[6]

[1]*State Key Laboratory of Nuclear Physics and Technology, School of Physics, and Fusion Simulation Center, Peking University, Beijing 100871, China*
[2]*Lawrence Livermore National Laboratory, Livermore, CA94550, USA*
[3]*School of Physics, Dalian University of Technology, Dalian 116024, China*
[4]*School of Engineering and Applied Physics, University of Science and Technology of China, Hefei 230026, China*
[5]*General Atomics, San Diego, CA92186, USA*
[6]*Department of Physics, Harbin Institute of Technology, Harbin 150001, China*

Corresponding authors: xu2@llnl.gov

Abstract:

Investigation of turbulent transport dynamics in Scrape-off-layer (SOL) and divertor heat flux width prediction is performed for ITER. Both BOUT++ transport and BOUT++ turbulence codes are applied to capture the physics on different temporal scales. Simulations start with an ITER 15MA baseline scenario profile generated by CORSICA [1]. In BOUT++ transport code, the plasma parameters (n_i, T_i, T_e) and radial electric (E_r) profiles are evolved to steady state. The initial plasma profiles inside the separatrix are taken from CORSICA scenario studies. Transport coefficients are calculated by inverting the plasma profiles inside the separatrix. SOL transport coefficients are assumed to be constants connected to the separatrix. A parametric scan for the anomalous thermal diffusivity (χ_i, χ_e) in the SOL is performed separately with $E \times B$ and magnetic drift included, and without any drift effects. The results show that when the diffusivity is smaller than a critical χ_{crit}, the heat flux width λ_q remains almost unchanged, which is roughly consistent with Goldston's heuristic drift model[2]. Otherwise, it increases as a $\lambda_q \propto \chi^{1/2}$ scaling resulting in a larger λ_q. BOUT++ six-field/two-fluid turbulence code is used to study pedestal and SOL turbulence dynamics and corresponding transport. In the turbulence simulation, pedestal is found to be peeling-ballooning unstable, which results in a larger λ_q. Pedestal structure is also found to be important in determining the effective thermal diffusivity and could lead to changes in the divertor heat flux width.

Key Words: ITER, heat flux width, transport, drift, turbulence

1. Introduction

One of great challenges to steady state operations of ITER and future magnetic confined fusion reactors is how to withstand the heat flux with the currently available materials, for both first walls and divertor targets. Design limit for maximum ITER divertor heat load is 10 MW m^{-2}, which requires a sizeable heat load width λ_q to handle the 100MW fusion power. Recent experimental scaling on multi-machine H-mode discharges shows that the heat load width follows reasonably well the $\lambda_q \sim 1/B_p^{\gamma}$ scaling, where γ is in the range from 1.11 to 1.27[3-5]. If the scaling works for future large machines, however, it would yield a very small $\lambda_q \cong 1mm$ mapped back to the outer-mid-plane (OMP) for ITER 15MA/Q=10 baseline scenario with $B_{p,omp} = 1.3T$, resulting in an intolerable heat load on the divertor target. Different theoretical models have also been derived. One of them is the well-known *Heuristic Drift Model* by R. J. Goldston[2], which can match pretty well with Eich's scaling on present experiments[4]. Numerical simulations have also been carried out to identify the achievable ITER divertor heat load width by varying the scape-off-layer(SOL) anomalous thermal diffusivity within realistic constraints in 2D transport code SOLPS[6, 7]. Above discussions show that the heat load width can be extremely small to threaten the survivability of ITER divertor targets, which is becoming a main concern for ITER steady state operation. Meanwhile, theoretical turbulence estimation by J. R. Myra[8] shows that λ_q may be enlarged by turbulence, such as interchange driven instabilities. Recent gyro-kinetic simulation performed by XGC1[9] also shows that the heat flux width λ_q could be as large as 5.9 mm. The result suggests that turbulence is important under ITER condition, and responsible for the enhancement of the heat flux width. An open question is then what relative roles drift and turbulence play in determining the heat flux width, and if they act in concert, or does one dominate over the other under ITER relevant condition.

BOUT++, a framework with a set of physics models[10,11], is widely used to simulate tokamak edge behavior, such as ELM dynamics[12, 13, 14] , SOL physics[15, 16, 17, 18] and neutral physics[19, 20, 21]. To capture the different physics in different temporal-scales, BOUT++ six-fields turbulence and transport simulation modules are developed separately with a similar set of Braginskii equations[15, 18]. Different modules have different foci: turbulence code mainly focuses on fast turbulence dynamics and scale of up to a few hundred Alfvén times; while the BOUT++ transport module mainly focuses on 2D plasma evolution to steady state on a longer transport time scale and includes the necessary pellet injection and neutral physics.

Nevertheless, coupling the two codes under a unified BOUT++ framework in the future could produce a promising integrated modeling platform[22]. We note that the ability to investigate divertor heat flux saturation is quite different for the two codes. BOUT++ transport module can reach both ion and electron heat flux saturation, while only the electron heat flux can reach saturation in BOUT++ turbulence code with realistic computing time due to the fast electron parallel thermal conduction[17]. The time solver becomes hard to converge if the simulation time is too long. Therefore within this limitation, we can get well-saturated electron divertor heat fluxes, but not easy for those of ions due to the slow ion parallel dynamics.

For this reason, our paper mainly focuses on electron dynamics in order to connect the results of the two codes. Using BOUT++ turbulence code, comparisons between simulation results and experimental data are performed for multiple current tokamaks, such as C-Mod[16, 17], EAST,[15] and DIIID[23], which yield a good agreement between numerical simulations and experiments, especially for λ_q. Similarly, the simulation results from BOUT++ transport code simulations also show a good agreement with C-Mod data, including E_r and λ_q [16, 17, 24]. These results contribute to the confidence in using both BOUT++ turbulence and transport codes to predict ITER heat flux width λ_q.

The layout of this letter is as follows. In section 2, we perform the BOUT++ transport simulations by changing anomalous thermal diffusivity. In section 3, BOUT++ six-field two-fluid turbulent simulation is carried out, including different upstream pedestal parameters. The results elucidate how λ_q is influenced by peeling-ballooning turbulence. Finally, the conclusion and discussions are presented in section 4.

Deleted: Numerical errors would accumulate so that the simulation cannot reach ion saturation state.

Formatted: Indent: First line: 0 ch

2. Different mechanisms in determining SOL heat flux width

It is well known that SOL heat flux width is determined by the competition between perpendicular cross field transport and parallel transport in SOL[25]. Different mechanisms contribute to the perpendicular cross field transport, such as drift, turbulence, collisions and ion orbit losses, etc., with the first two being the main contributors . To evaluate the impact of different mechanisms, theoretical models have been developed by separately considering drift[2] and turbulence[8], and numerical simulations are being carried out with 2D transport code SOLPS[6, 7],UEDGE[26] and reduced model[27], fluid code GBS[28], GDB[29,30] and gyro-kinetic code XGC1[9]. In this section, we present results from BOUT++ transport code, which includes $E \times B$ and magnetic drift physics, and ad hoc radial transport coefficients to model the turbulence cross field transport. The ITER geometry, simulation settings and transport coefficient scan in the SOL are shown in Sec. 2.1. Separatrix temperature scan and implications of results would be discussed in Sec. 2.2 and Sec. 2.3, respectively.

2.1 Anomalous thermal diffusivity scan in SOL

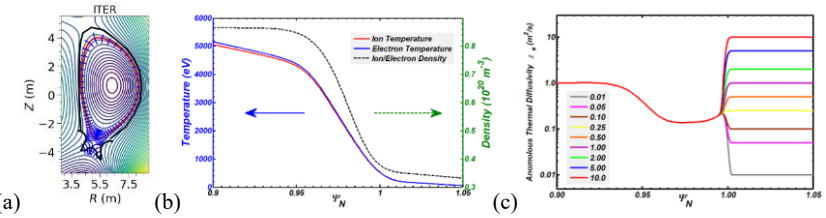

(a) (b) (c)

Figure 1. (a) ITER 15MA baseline scenario geometry and grid setting in BOUT++ simulation; (b) ITER plasma kinetic profiles including ion density, ion and electron temperature profile used in simulation; (c) Anomalous electron thermal diffusivity setting and scan in SOL.

The simulation grid-file and plasma profiles are generated from the 2015 ITER 15MA baseline scenario with Be/Ar impurities case previously constructed by CORSICA[1], which has a steeper pedestal density gradient compared with previous ITER profiles[31]. Fig. 1 (a) shows the geometry with radial and poloidal grid cells in the simulation. Simulation domain in normalized poloidal flux is $0.9 < \Psi_N < 1.05$ and grid resolution is $n_\psi = 256, n_y = 64$, shown as the short blue lines in Fig. 1 (a), which is fine enough to capture the physics in fluid model, $\rho_i/\delta x \sim 1$. CVODE is used as the time solver for time evolution[32]. Plasma kinetic profiles are shown in Fig. 1 (b), where density and temperature profiles inside the separatrix

are taken from a previous scenario study and extrapolated into the SOL region. Sheath boundary conditions are applied on the both divertor target[16-18] and inner boundary in radial direction of density and temperatures are set to be same as initial value $n_{in} = n_{in,t=0}$, while outer boundaries are set to be Neumann, i.e. $\partial n/\partial \psi = 0$ to let them freely evolve. Radial thermal diffusivity χ_e is shown in Fig. 1 (c), which are inverted from steady state transport equations without drifts using initial plasma kinetic profiles and are assumed to be unchanged in the core/pedestal region[18]. Meanwhile they are varied over a wide range in the SOL, from 0.01 to 10.0, to study the effects of changing turbulence transport magnitude on divertor heat flux width λ_q, where we do not specify what kind of turbulence it is. Ion thermal transport coefficient χ_i , in the core/pedestal region is also inverted from ion density and temperature profiles and takes on the same value as χ_e in SOL. Anomalous particle thermal diffusivity $D_\perp$ is inverted from steady state continuity equation using initial density profile and kept fixed in the whole simulation domain when doing the $\chi_{i,e}$ scan.

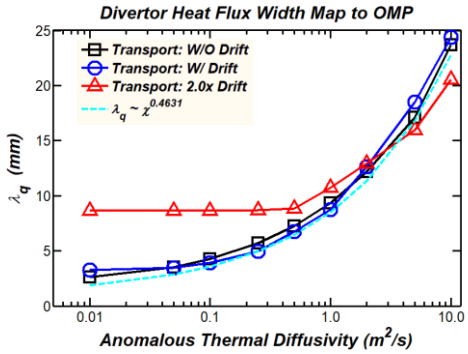

Figure 2. The outer divertor heat flux width $\lambda_q$vs the SOL anomalous thermal diffusivity $\chi_{i,e}$. The outer divertor heat flux width is mapped to outer-mid-plane (OMP) for $T_{sep} =$ 500eV.

In Fig. 2, the horizontal axis shows anomalous thermal diffusivity setting in our simulation and the vertical axis is the outer divertor electron heat flux width mapped back to the outer-mid-plane (OMP), which is fitted using Eich's fitting formula given by Eq. (1), and parallel heat flux and the distance in the OMP are used in the fitting. The definitions of various quantities are given in[3].

$$q(\bar{s}) = \frac{q_0}{2}\exp\left[\left(\frac{S}{2\lambda_q f_x}\right)^2 - \frac{\bar{s}}{\lambda_q f_x}\right]\mathrm{erfc}\left(\frac{S}{2\lambda_q f_x} - \frac{\bar{s}}{S}\right) + q_{BG} \quad (1)$$

Where $\bar{s} = s - s_0 = (R - R_{sep}) \cdot f_x$, s is the radial path length along target, s_0, the strike line position at target, f_x, magnetic flux expansion factor, q_{BG}, background heat flux, S, divertor spreading factor and the peak heat flux q_0. The solid black curve with squares shows the case without drifts, i.e. we turned off the $E \times B$ and magnetic drifts and we only keep the anomalous thermal diffusion as the source of perpendicular cross field particle/heat flux. The curve has a monotonically increase as $\chi_{i,e}$ increases. It agrees quite well with a $\chi^{1/2}$ scaling depicted by the cyan dashed curve. This scaling can be simply derived by a balance between radial and parallel fluxes in steady state, i.e. $\nabla \cdot q = 0$, and assuming the linear relation $\lambda_q = \frac{2}{7}\lambda_T$ in the conduction-limit[5, 7]. The blue solid curve with circles is the result when taking the drift terms into consideration and it shows a small deviation at the small $\chi_\perp$ regime. When $\chi_\perp < 0.1\,m^2/s$, λ_q stays nearly unchanged; while for $\chi_\perp$ exceeding $0.1\,m^2/s$, the solid blue curve would increase monotonically and show the same trend as the case without drifts. The flat region is clearly visible if we doubled the drift effect by multiplying the $E \times B$ and magnetic drift terms by a factor of 2, as shown by the red solid curve with triangles in Fig. 2. This results in a clearly visible flat region with λ_q increasing by a factor of 2, and the turning point for $\chi_\perp$ corresponding to the upturn in λ_q increases to $0.5m^2/s$. This heuristic exercise shows that larger drifts can increase λ_q and expand the drift-dominated region by moving the transition $\chi_\perp$ to a larger value. A competition exists between drift and turbulence in determining the perpendicular cross field thermal transport. The drifts set a lower limit λ_q for a quiescent SOL when $\chi_\perp$ is small, which is narrow for realistic drifts and detrimental to a divertor. Conversely, a turbulence dominated SOL could enlarge λ_q and spread the heat load to the divertor plate. The conditions under which the SOL would transition into a turbulent regime are thus crucial for developing a divertor heat exhaust solution.

2.2 Separatrix temperature scan and comparison with Heuristic Drift Model

In the previous section 2.1, we showed the thermal diffusivity scan for $T_{sep} = 500\mathrm{eV}$ and increased the drift effect by a constant value of 2 to illustrate the transition. A physical mechanism to affect the magnetic drift will be discussed in this section. We know that the

drift contributes to perpendicular cross field transport is proportional to the Maxwellian-averaged magnetic drift velocity $\langle v_{\mathrm{grad}B+\mathrm{curv}B}\rangle = {}^{2T_{sep}}/_{eBR}$[2], where $v_{\mathrm{grad}B+\mathrm{curv}B}$ is the drift velocity due to gradient *B* and curvature *B* drift, *B* and *R* are the toroidal magnetic field in Tesla and major radius in meters, respectively, and ${}^{T_{sep}}/_{e}$ is the temperature in electron-volts at the separatrix. It is well established that gas puffing and controlled impurity injection in the SOL could modify T_{sep} and hence the drift behavior. To study this effect, we keep the core temperature unchanged while varying the separatrix temperature, which extrapolates into the SOL region to change the drift magnitude, and its impaction on Goldston's *heuristic drift model*.

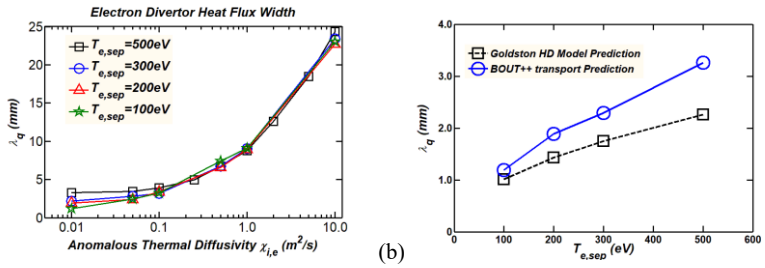

(a) (b)

Figure 3. (a) Divertor heat flux width as a function of anomalous thermal diffusivity $\chi_{i,e}$ with different separatrix temperature. (b) Comparison with Goldston's heuristic drift model.

The result from different separatrix temperature scan is shown in Fig. 3 (a). Different color curves, green, red, blue and black, correspond to separatrix temperatures of 100eV, 200eV, 300eV and 500eV, respectively. We can see a clear trend that the flat region becomes larger and more obvious when the temperature increases, which means the drift becomes more important in the radial transport. In Fig. 3 (b), a λ_q comparison between simulated with BOUT++ at $\chi_\perp = 0.01\, m^2/s$ and Goldston's heuristic drift model for different separatrix temperature is presented. These two curves bear a similar trend, with the BOUT++ λ_q diverging to higher values as T_{sep} becomes large. In the simulation, the averaged parallel flow from OMP to X-point is calculated to be around $0.3 - 0.4C_s$, which is smaller compared with an estimate of $0.5C_s$ in Goldston's model. A slower parallel flow would result in a longer transit time in the SOL, because of $\lambda_q \sim \langle V_{dr}\rangle \tau_{tran}$, where $\langle V_{dr}\rangle$ is the averaged radial drift velocity and τ_{tran} is the transit time.

198

199 *2.3 Simple scaling from drift dominated to turbulence dominated regime*

200 In Sec. 2.1, we have identified a drift dominated and a turbulence dominated regime in

201 determining the divertor heat flux width λ_q. In the small $\chi_\perp$ limit, λ_q can roughly match

202 Goldston's heuristic drift model. In the large $\chi_\perp$ regime, λ_q would follow a scaling of

203 $\sim {\chi_\perp}^{1/2}$. Here we derive a simple scaling for the critical $\chi_{\perp,crit}$ for turbulence at the

204 transition between drift and turbulence dominated regime, which is used to highlight the

205 influence of key plasma parameters.

206 The effective thermal diffusivity for radial drift flux is,

207 $$nv_{\mathrm{gradB+curv}B}T \sim -n\chi_{eff}\nabla_\perp T \sim n\chi_{eff}T/\lambda_T \quad (2),$$

208 where *n* and *T* are the separatrix density and temperature, respectively, λ_T is the temperature

209 fall of length, and using the electron drift velocity $\langle v_{\mathrm{grad}B+\mathrm{curv}B}\rangle = {2T_{sep}}/{eBR}$ from

210 previous section, we can get the critical $\chi_{\perp,crit}$ for turbulence by assuming the balance

211 between turbulence and drift radial flux,

212 $$\chi_{crit} \sim \chi_{eff} \sim \frac{2T}{eBR}\lambda_T \quad (3)$$

213 In the SOL, we use a relationship between λ_T and λ_q[5, 7]. For example, by considering a

214 fully convective and a fully conductive parallel transport, there are two different limits,

215 $$\lambda_q = \begin{cases} \left(\frac{1}{\lambda_n} + \frac{3}{2}\frac{1}{\lambda_T}\right)^{-1} < \frac{2}{3}\lambda_T, convection\ limit \\ \frac{2}{7}\lambda_T,\ conduction\ limit \end{cases} \quad (4)$$

216 For simplicity, we assume Goldston's heuristic drift model remains valid up to the critical

217 value χ_{crit}, i.e. $\lambda_q \sim \frac{4a}{B_p R}\left(\frac{m_p}{e}\right)^{\frac{1}{2}} T^{\frac{1}{2}}$. By substituting this expression into Eq. (4) to solve for

218 λ_T, we can get an expression for χ_{crit} using Eq. (3) as,

219 $$\chi_{crit} \in \left[\frac{12a}{BB_pR^2}\left(\frac{m_p}{e^3}\right)^{\frac{1}{2}} T_{sep}^{\frac{3}{2}},\ \ \frac{28a}{BB_pR^2}\left(\frac{m_p}{e^3}\right)^{\frac{1}{2}} T_{sep}^{\frac{3}{2}}\right] \quad (5)$$

220

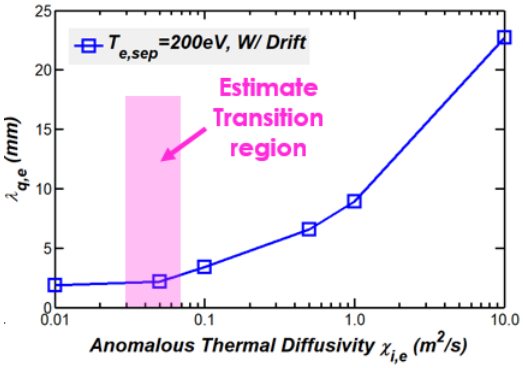

Figure 4. Blue curve shows the scan of transport coefficient for $T_{sep} = 200eV$ and the pink shade region shows estimated transition region between drift and turbulence.

The region specified by Eq. (5) is highlighted by the pink shaded region in Fig. 4. It sits roughly at the transition region as expected. This simple model can apply to different separatrix temperatures T_{sep}, like for $T_{sep} = 500eV$, the estimated critical $\chi_\perp$ would be in the range of [0.12, 0.28], which can roughly cover the turning point of the black curve in Fig. 3 (a). From Eq. (5), χ_{crit} is proportional to $T_{sep}^{\frac{3}{2}}$, indicating that the drift dominated region would be larger if T_{sep} increases, which is consistent with Fig 2 and Fig. 3 (a). Other important geometric parameters are B, B_p and R in the denominator, hence χ_{crit} would decrease when B, B_p and R increase. It suggests that ITER might have a relatively small χ_{crit} and turbulence would likely dominate cross-field transport in the SOL for ITER. To provide a more quantitative value of turbulent $\chi_\perp$ for ITER SOL, we will use BOUT++ six-field two-fluid module to conduct the simulations in section 3.

3. Turbulence dynamics for ITER 15MA baseline scenario

In this section, we will use BOUT++ six-field two-fluid turbulence model to simulate the same ITER 15MA baseline scenario geometry and study the turbulence dynamics. Density n, ion/electron temperature T_i/T_e, ion parallel velocity $V_{i\parallel}$, vorticity $\varpi = \boldsymbol{b_0}\cdot\nabla\times\boldsymbol{V}_\perp$ and parallel magnetic vector potential $A_\parallel$ are evolving variables in BOUT++ six-field turbulence model. Simulation grid and geometry are the same as those used in the BOUT++ transport module in Sec. 2, and the boundary conditions are also the same, with a sheath boundary condition applied at the divertor target. In the core inner boundary at $\psi_N = 0.90$, a self-adjusted heat flux is applied to keep the pedestal top profile approximately unchanged while the pedestal and SOL profiles can freely evolve. The turbulence dynamics of ITER 15MA baseline scenario will be discussed in Sec. 3.1. Effect of different upstream pedestal height on the divertor heat flux width will be elucidated in Sec. 3.2.

3.1 Turbulence dynamics of ITER 15MA baseline scenario

The BOUT++ six-field two-fluid module, which is based on Braginskii equations, includes a variety of physics processes, such as peeling-ballooning mode, acoustic wave and drift Alfvén wave. The parallel thermal conductivity in the flux limited form is given by,

$$\kappa_{eff,j} = \frac{\kappa_{\parallel,j}^{SH}\kappa_{\parallel,j}^{FS}}{\kappa_{\parallel,j}^{SH}+\kappa_{\parallel,j}^{FS}} \quad (6)$$

, where j signifies ion or electron, $\kappa_{\parallel,i}^{SH} = 3.9 n_i v_{th,i}^2/\nu_i$ and $\kappa_{\parallel,e}^{SH} = 3.2 n_e v_{th,e}^2/\nu_e$ are the Spitzer-Härm parallel thermal conductivities, $v_{th,j}$ and ν_j are the thermal velocity and collision rate for the j species. $\kappa_{\parallel,j}^{FS} = \alpha_j n_j v_{th,j} q R_0$ is the free streaming parallel thermal conductivity, where q is the safety factor and R_0 is the major radius.Here, α_j is a free-streaming factor, which is typically in the range of $[0.03,\ 0.3]$ from kinetic simulations[33]. We assume $\alpha_i = \alpha_e = 0.1$ in our simulations, which means more toward to the collisonless regime. A detailed scan for this parameter can be found in previous papers[15, 16]. Resistivity η is considered as Spitzer-Härm resistivity and hyper-resistivity is taken as a constant value $\eta_H = 10^{-16}$ in generalized Ohm's law for current diffusion. The E_r calculated from ion pressure gradient (diamagnetic E_r) is also used in the simulation.

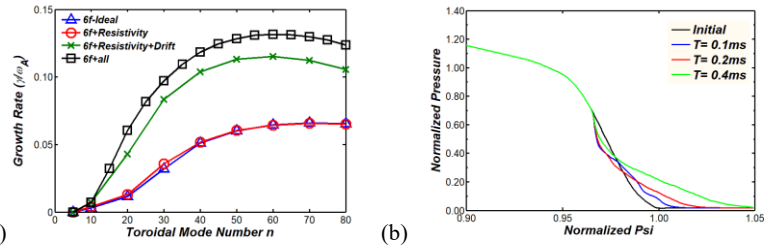

Figure 5. (a) Linear growth rate of ITER 15MA baseline scenario. (b) Outer-mid-plane pressure profile evolution at different time slices.

From linear simulation results in Fig. 5 (a), where the blue curve with triangles is the linear growth rate of ideal peeling-ballooning mode using six-field two-fluid code, red curve with circles is the linear growth rate taking Spitzer resistivity into consideration. We further consider the parallel gradient of electron pressure in magnetic vector perturbation equation to capture the drift-alfvén instability in green curve with cross and the black cure with squares including the full fluid physics. We find that the ideal ballooning and drift-alfvén instability are the dominated instabilities and the most unstable toroidal mode numbers are at high n. We cut off the toroidal mode at n=80 because $k_\theta \rho_i$ is around 0.3 for n=80, which means the fluid reduction might be invalid when n becomes larger. Therefore, initially the ITER 15 MA baseline scenario is driven unstable by a ballooning-drift mixed type mode with the most unstable mode at the outer-mid-plane. A similar feature can be also found in the linear stage of our nonlinear simulation, Fig. 6 (a). Fig. 5 (b) shows the pressure profile evolution at the outer-mid-plane and as stated the pedestal top is kept unchanged, while the outer profile freely evolves and finally crashes to flatten the pedestal gradient in ~0.4ms. This indicates a lot of thermal energy irreversibly escapes from the pedestal region to the SOL, the detailed amount of which will be evaluated next.

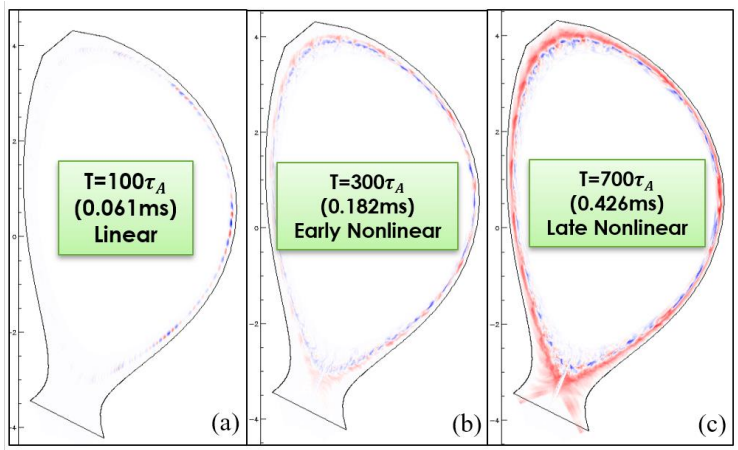

Figure 6. Contour plot of perturbed pressure in $\zeta = 0$ poloidal slice at different time slices.

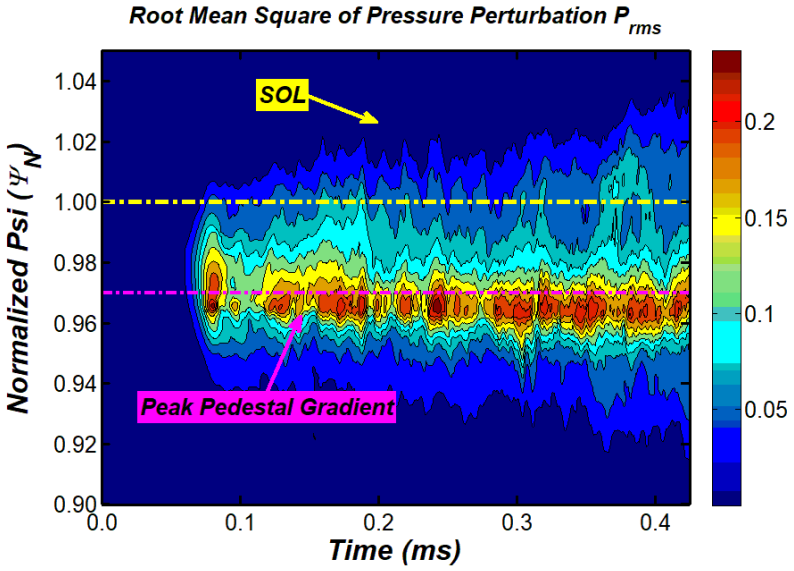

Figure 7. The contour plot for root mean square of pressure perturbation at outer-mid-plane (OMP).

Fig. 6 and Fig. 7 show the turbulence spreading process in our simulation, where $1\tau_A = 0.608\mu s$. In Fig. 6 (a), the initial perturbation is localized at the low field side (LFS) inside the separatrix and shows a ballooning type mode, where the dominated toroidal mode number $n\sim45$. At later time, turbulent fluctuation then spread across the separatrix and go into the

SOL region in Fig. 6 (b). At even longer time, SOL parallel transport along the open field lines carries energy and particles towards the divertor in Fig. 6 (c). Fig. 7 clearly shows that the perturbation at the outer-mid-plane (OMP) is generated at the peak pedestal gradient location and spreads into the SOL, and similar trend is found at other poloidal locations, such as upper and lower part of low-field-side and mid-plane of high-field-side. This indicates that, for the ITER 15MA baseline scenario, the SOL turbulence is generated from the upstream pedestal region, and not by local instabilities in our simulation.

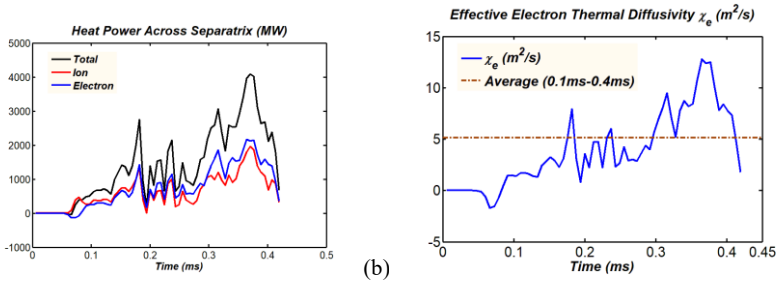

(a) (b)

Figure 8. (a) $E \times B$ turbulence induced power across separatrix; (b) Effective electron thermal diffusivity as a function of time.

Fig. 8 (a) shows the heat power across separatrix by $E \times B$ turbulent convection. The definition of perpendicular ion and electron heat flux is,

$$q_{ir,tur} = n_i T_i \frac{(\boldsymbol{b_0}\times\nabla\phi)_r}{B_0}, q_{er,tur} = n_e T_e \frac{(\boldsymbol{b_0}\times\nabla\phi)_r}{B_0} \quad (7)$$

, where, $\boldsymbol{b_0}$ is the unit vector of magnetic field and ϕ is electric potential. Power across separatrix is the integral of flux over the separatrix surface in poloidal and toroidal direction, $Q_{sep,j} = \oiint q_{jr,tur}$. Taking an average over the saturated time period of the turbulence from $200\tau_A$(0.122ms) to $700\tau_A$(0.426ms), we get $\langle Q_{sep,t}\rangle_t = 1.758GW$, which is much larger than the injected power ~100MW for the scenario being considered. The loss of such a large amount of thermal energy in a short time period ~0.4ms implies that the pedestal cannot be re-established quickly. This is a typical characteristic of Type-I ELMs. In Fig. 8 (b), the effective electron thermal diffusivity is calculated, where the blue solid curve is χ_e as a function of time and the brown dash-dotted line is the time averaged $\chi_e = -\left\langle \frac{\langle q_{tur}\rangle_{\theta\zeta}}{\langle n\nabla T\rangle_{\theta\zeta}} \right\rangle_t = 5.15\, m^2/s$ over the same period as the heat power calculation. A large $\chi_e \gg$

χ_{crit}~$0.05\,m^2/s$ indicates that the ITER 15MA baseline scenario is likely in the turbulence dominated regime.

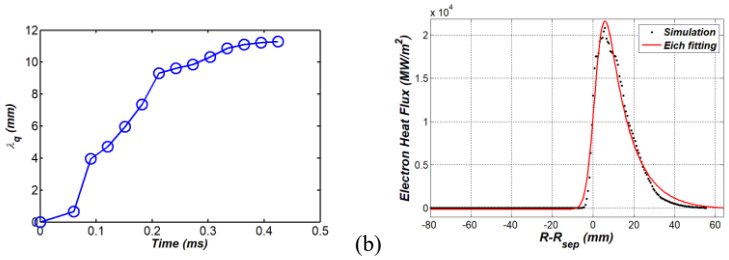

(a) (b)

Figure 9. (a) Calculated λ_q vs. simulation time; (b) Outer divertor heat flux mapped back to outer-mid-plane(OMP).

The evolution of λ_q in time is given in Fig. 9 (a), showing that λ_q saturates around 0.35ms. In Fig. 9 (b), the horizontal axis is the distance away from the separatrix at the OMP and the vertical axis is divertor electron heat flux. The small black dots are simulation results and the red solid curve is the fitting curve using Eich's fitting shown in Eq. (1). Eich's fitting formula yields a $\lambda_q = 11.28mm$ and a spreading factor $S = 5.05mm$. Our results show that a ballooning type instability would produce a large effective electron thermal diffusivity χ_e and consequently increase the peak heat flux and broaden the divertor heat flux decay width λ_q. This has also been predicted in J. R. Myra's paper[8], where an interchange driven instability would result in a much larger divertor heat flux decay width λ_q for ITER.

3.2 Effect of upstream pedestal height on determining λ_q

It is also of interest to ask what the value of λ_q would be if the energy loss by ELM is weak such as in a small-ELM regime. To investigate that, we lower the pedestal height to vary the peeling-ballooning turbulent drive and calculate the corresponding divertor heat flux and λ_q. We decrease the pedestal height by multiplying a factor, from 1.00 to 0.80, in front of the pressure and parallel current, and recalculate the MHD equilibrium using CORSICA. The poloidally averaged pressure and parallel current profiles are shown in Fig. 10 (a). In Fig. 10 (b), the linear growth rate with different pedestal heights are presented. The most unstable

mode would change in the range of n=50-80 for different pedestal heights but high-n ballooning mode would dominate in these cases.

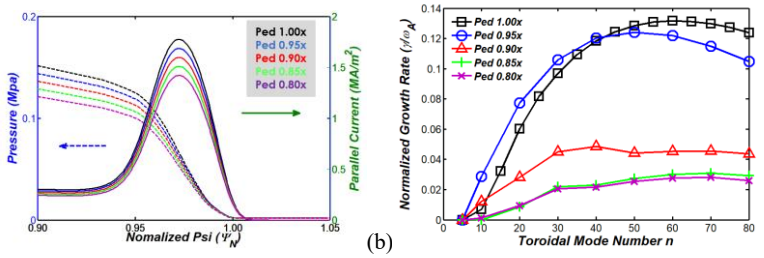

(a) (b)

Figure 10. (a) Pressure and parallel current profile with different pedestal heights; (b) linear growth vs. toroidal mode number for different pedestal heights.

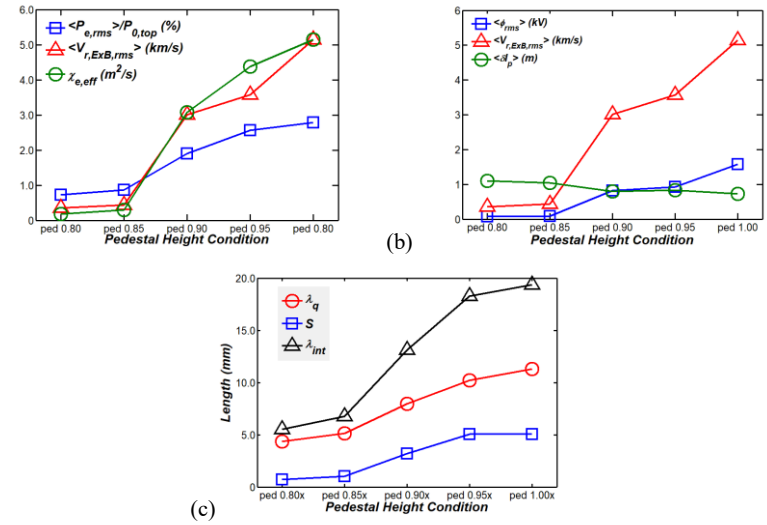

(a) (b) (c)

Figure 11. (a) Electron pressure (blue) and radial $E \times B$ velocity (red) perturbation and effective thermal diffusivity χ_e (green) at separatrix for different pedestal heights; (b)Electrostatic potential, radial $E \times B$ velocity and effective poloidal correlation length at separatrix for different pedestal heights; (c) Heat flux width λ_q, spreading factor S and integrated heat flux width λ_{int} for different pedestal heights.

Turbulence perturbation at separatrix is shown in Fig. 11 (a), where subscript rms means root-mean-square average in toroidal direction and bracket <…> is taking poloidal and time

average during saturated state for each case. Blue line with squares shows the electron pressure perturbation, red line with triangles shows the radial $E \times B$ velocity perturbation and effective electron thermal diffusivity χ_e is shown as green curve with circles. These indicate that turbulence intensity and radial $E \times B$ velocity work together in determining the radial thermal transport. Radial $E \times B$ velocity would be determined by electrostatic potential and poloidal correlation length of electrostatic potential $V_{r,E\times B} = \boldsymbol{b} \times \nabla\phi/B \sim \phi/\delta l_p B_T$. In Fig.11 (b), we show the electrostatic potential ϕ (blue curve with squares), radial $E \times B$ velocity (red curve with triangles) and effective poloidal correlation length δl_p (green curve with circles) ,which is defined as $\langle \delta l_p \rangle = \langle \phi_{rms}/V_{r,E\times B,rms} \times B_T \rangle$ and <…> also means poloidal and time average. We can see a weak decreasing trend in $\langle \delta l_p \rangle$ when pedestal height increases. We know that δl_p related to the saturated toroidal mode number n $\delta l_p \sim 2\pi a\sqrt{\frac{1+\kappa^2}{2}}/m \sim 2\pi a\sqrt{\frac{1+\kappa^2}{2}}/nq$, it means that different pedestal condition would have different toroidal n in saturation state. A more detailed analysis of turbulence including toroidal n mode number in saturated state, relative phase between pressure and electrostatic potential and their effects on determining radial thermal transport would be shown in the future. In Fig. 11 (c), the red solid curve with circles heat flux width λ_q mapped to the OMP, the blue curve with squares is the spreading factor in Eich's fitting formula and the black curve with triangles is the integral heat flux width at the outer divertor target, which is defined by a simple form $\lambda_{int} = \lambda_q + 1.64S$ [34]. All three curves exhibit a similar trend that the width increases with pedestal height, with a range from 4mm to 12mm. For the low pedestal height, 0.80/0.85 of the original pedestal height, λ_q lie in the weak turbulence regime, although it is still twice as large as the value from Goldston's model. The other three cases with factors of 0.90, 0.95 and 1.00 probably would fall into the peeling-ballooning turbulence dominated regime. For each pedestal height, we can calculate the turbulent thermal diffusivity as shown in Fig.8 (b) and the divertor heat flux width as shown in Fig. 9 (b). The combined λ_q from turbulence and transport simulations are shown in Fig. 12.

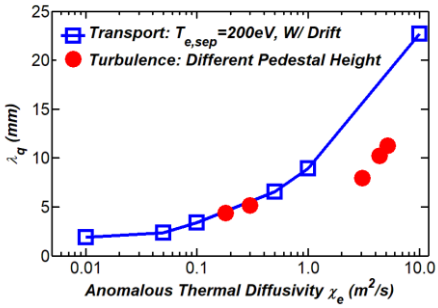

Figure 12. Comparison between BOUT++ transport and BOUT++ turbulence results.

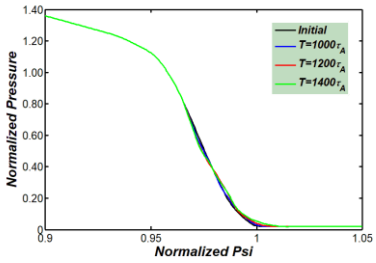

Figure 13. Pressure Profile evolution in the Out-mid-plane(OMP) for 0.85 pedestal case.

The blue solid curve with squares is the result with a separartrix temperature equals to 200eV, which is the same as the curve in Fig. 3 (a) and Fig. 4. The red bullets are the results with corresponding effective thermal diffusivity $\chi_\perp$ and heat flux width λ_q from turbulence simulation with different pedestal heights. For the pedestal height with a factor of 0.80/0.85, where turbulence transport becomes weaker and weaker, the λ_q points lie on the transport curve, and they are in the weak turbulence regime, where the pedestal plasma profiles are marginal unstable, which leads to continuous turbulence transport. Although the other three red bullets show a similar trend as the blue curve, instead they lie below the transport blue curve. There are two possible reasons for this deviation:

(1) In BOUT++ transport code, the core/pedestal transport coefficients are kept unchanged implying that the plasma is still in an original H-mode state in the scan of transport coefficient $\chi_\perp$ in SOL; whereas, in turbulence code, they are no longer in the original H-mode state and large ELM crash would cause the profile in the bottom of pedestal to be flattened. Hence, it may not be an apple-to-apple comparison for the last three points,

404 0.90/0.95/1.00. The fact that the first two points lie on the blue curve supports this
405 argument, because their pressure profiles are almost unchanged during simulation, as
406 Fig. 13 shows for 0.85 times pedestal height case;
407 (2) Another possibility is that turbulence generated by nonlocal transport may not follow the
408 Ficksian transport model used in Sec 2.
409
410 These two conjectures would be interesting topics for future investigations[35].
411

4. Summary and Conclusion

A detailed study of divertor heat flux width for ITER 15MA baseline scenario is performed on both BOUT++ transport and BOUT++ six-field turbulence module, with an objective to improve the prediction on the important issue of ITER divertor heat flux width. In Sec. 2, we found that drift and turbulence tend to compete in determining the perpendicular cross field transport and as a result produce very different heat flux widths in the region where they are dominant. The connection between the two might bridge the gap between the small λ_q given by experimental scaling and large λ_q from turbulence theory and simulation. Specifically, when $\chi_\perp$ is smaller than a critical value $\chi_{\perp,crit}$, drift would dominate the perpendicular transport and λ_q can roughly match the Goldston's heuristic drift model; when $\chi_\perp$ is greater than $\chi_{\perp,crit}$, turbulence would take over and λ_q would increase monotonically and follows the simple scaling $\lambda_q \sim \chi_\perp^{1/2}$. A simple model is derived to determine the critical thermal diffusivity for the transition region between drift and turbulence dominated regime, $\chi_{\perp,crit} \sim T_{sep}^{\frac{3}{2}} \Big/ BB_p R^2$, which indicates that the current machines with smaller major radius and lower current or poloidal magnetic field might have a larger $\chi_{\perp,crit}$ and probably lie in the drift dominated region. For future machines, with a larger major radius and a higher magnetic field, $\chi_{\perp,crit}$ is reduced and turbulence might become the main contributor to the perpendicular transport and hence the main determinator of λ_q.

In Sec. 3, the BOUT++ six-field two-fluid turbulence code is applied to the ITER 15MA baseline scenario. We find that the pedestal is unstable by ballooning-drift mixed type instability and a large ELM crash would occur. This pushes ITER into the turbulence dominated regime and results in a large $\lambda_q = 11.28mm$, which has been predicted by previous turbulence theory. We also carried out a pedestal height scan and find that both heat flux across separatrix and heat flux width λ_q are sensitive to upstream pedestal height. Comparison is also made between BOUT++ transport and turbulence code. The two code results can roughly match each other with some deviations.

Last but not the least, we find that the peak heat flux on the divertor target is still large even with an enhanced λ_q. This is caused by an increase of total heat power across separatrix from

the type-I ELMy H-mode plasmas. Two approaches are strong candidates to mitigate this issue: (1) Operate with grassy-ELMs where the energy escaping the core is frequent but small; and (2) Operate with divertor detachment using gas puffing and control impurity injection, which can further reduce the peak heat flux at the divertor target.

Appendix: Six-fields equations used in BOUT++ transport and turbulence model

1. BOUT++ transport model

$$\frac{\partial N_i}{\partial t} = -\nabla_\parallel(V_{\parallel i}N_i) + \boldsymbol{\nabla}_\perp \cdot (D_\perp \boldsymbol{\nabla}_\perp N_i) - \boldsymbol{\nabla} \cdot (N_i \boldsymbol{V_{E\times B}}) - \boldsymbol{\nabla} \cdot \left(N_i \boldsymbol{V_{dia}^i}\right) \quad \text{(App. Eq. 1)}$$

$$\frac{\partial T_i}{\partial t} = -V_{\parallel i}\nabla_\parallel T_i - \frac{2}{3}T_i\nabla_\parallel V_{\parallel i} + \frac{2}{3N_i}\nabla_\parallel(k_{\parallel i}\nabla_\parallel T_i) + \frac{2}{3N_i}\boldsymbol{\nabla}_\perp(N_i\chi_{\perp i}\boldsymbol{\nabla}_\perp T_i) + \frac{2T_i}{3}\boldsymbol{\nabla}_\perp \cdot \left(\frac{D_\perp}{N_i}\boldsymbol{\nabla}_\perp N_i\right) +$$

$$\frac{D_\perp}{N_i}\boldsymbol{\nabla}_\perp N_i \cdot \boldsymbol{\nabla}_\perp T_i - \boldsymbol{V_{E\times B}} \cdot \boldsymbol{\nabla} T_i \; - \frac{2}{3}T_i\nabla \cdot \boldsymbol{V_{E\times B}} - \frac{2}{3}T_i\nabla \cdot \boldsymbol{V_{dia}^i} - \frac{5T_i}{3Z_i e}\boldsymbol{\nabla} \cdot \left(\frac{1}{B_0}\boldsymbol{b_0} \times \boldsymbol{\nabla} T_i\right) +$$

$$\left(\frac{2m_e}{M_i}\right)\frac{T_e - T_i}{\tau_e} \quad \text{(App. Eq. 2)}$$

$$\frac{\partial T_e}{\partial t} = \frac{2}{3N_i}\nabla_\parallel(k_{\parallel e}\nabla_\parallel T_e) + \frac{2}{3N_i}\boldsymbol{\nabla}_\perp(N_i\chi_{\perp e}\boldsymbol{\nabla}_\perp T_e) + \frac{2T_e}{3}\boldsymbol{\nabla}_\perp \cdot \left(\frac{D_\perp}{N_i}\boldsymbol{\nabla}_\perp N_i\right) + \frac{D_\perp}{N_i}\boldsymbol{\nabla}_\perp N_i \cdot \boldsymbol{\nabla}_\perp T_e - \boldsymbol{V_{E\times B}} \cdot$$

$$\boldsymbol{\nabla} T_e - \frac{2}{3}T_e\boldsymbol{\nabla} \cdot \boldsymbol{V_{E\times B}} - \frac{2}{3}T_e\boldsymbol{\nabla} \cdot \boldsymbol{V_{dia}^e} + \frac{5T_e}{3e}\boldsymbol{\nabla} \cdot \left(\frac{1}{B_0}\boldsymbol{b_0} \times \boldsymbol{\nabla} T_e\right) - \left(\frac{2m_e}{M_i}\right)\frac{T_e - T_i}{\tau_e} \quad \text{(App. Eq. 3)}$$

$$\frac{\partial V_{\parallel i}}{\partial t} = -V_{\parallel i}\nabla_\parallel V_{\parallel i} + \frac{4}{3N_i M_i}\nabla_\parallel(\eta_i\nabla_\parallel V_{\parallel i}) + \frac{D_\perp}{N_i}\boldsymbol{\nabla}_\perp N_i \cdot \boldsymbol{\nabla}_\perp V_{\parallel i} - \frac{\nabla_\parallel P}{N_i M_i} - \boldsymbol{V_{ExB}} \cdot \boldsymbol{\nabla} V_{\parallel i} \quad \text{(App. Eq. 4)}$$

$$\frac{\partial \varpi}{\partial t} = B_0\nabla_\parallel J_\parallel + \mu_{i,\parallel}\nabla_\parallel^2\varpi + \mu_{i,\perp}\boldsymbol{\nabla_\perp^2}\varpi + \boldsymbol{\nabla} \cdot (2P\boldsymbol{\nabla} \times \boldsymbol{b_0}) - \boldsymbol{V_{ExB}} \cdot \boldsymbol{\nabla}\varpi + \frac{D_\perp}{N_i}\boldsymbol{\nabla}_\perp N_i \cdot \boldsymbol{\nabla}_\perp \varpi$$

(App. Eq. 5)

$$J_\parallel = -\frac{1}{\eta}\nabla_\parallel\phi + \frac{1}{\eta e N_i}\nabla_\parallel P_e + \frac{0.71k_B}{\eta e}\nabla_\parallel T_e \quad \text{(App. Eq. 6)}$$

Where, density N_i, ion/electron temperature T_i/T_e, ion parallel velocity $V_{\parallel i}$, parallel current $J_\parallel$ and vorticity ϖ are evolved to steady state and vorticity is defined as $\varpi = \frac{N_i M_i}{B_0}\left(\nabla_\perp^2\phi + \frac{1}{Z_i e N_i}\nabla_\perp^2 P_i + \frac{1}{N_i}\nabla_\perp N_i \cdot \nabla_\perp\phi\right)$. $\boldsymbol{V_{E\times B}} = \frac{1}{B_0}\boldsymbol{b_0} \times \boldsymbol{\nabla}\phi$ is the ExB velocity and $\boldsymbol{V_{dia}^{j=i,e}} = \frac{1}{Z_j q_j N_j B_0} = \boldsymbol{b_0} \times \boldsymbol{\nabla} P_j$ is the diamagnetic drift of ion and electron. $k_{\parallel i} = \frac{125P_i}{32M_i\nu_i}$ and $k_{\parallel e} = 3.16\frac{P_e}{m_e\nu_e}$ are the Spitzer-Härm parallel thermal diffusivity. $D_\perp$, $\chi_{\perp i}$ and $\chi_{\perp e}$ are the artificial particle/thermal perpendicular diffusivity to the represent turbulence effect. More details about BOUT++ transport model can be found in Ref. [18].

2. BOUT++ turbulence model

$$\frac{\partial n_i}{\partial t} = -\left(\frac{1}{B_0}\boldsymbol{b} \times \boldsymbol{\nabla}_\perp\phi + V_{\parallel i}b\right) \cdot \boldsymbol{\nabla} n_i - \frac{2n_i}{B_0}\boldsymbol{b} \times \boldsymbol{\kappa} \cdot \left(\boldsymbol{\nabla}_\perp\phi + \frac{1}{Z_i e n_i}\boldsymbol{\nabla} P_i\right) - n_i B_0 \nabla_\parallel\left(\frac{V_{\parallel i}}{B_0}\right)$$

(App. Eq. 7)

$$\frac{\partial T_i}{\partial t} = -\left(\frac{1}{B_0}\boldsymbol{b} \times \boldsymbol{\nabla}_\perp\phi + V_{\parallel i}b\right) \cdot \boldsymbol{\nabla} T_i - \frac{2}{3}T_i\left[\frac{2n_i}{B_0}\boldsymbol{b} \times \boldsymbol{\kappa} \cdot \left(\boldsymbol{\nabla}_\perp\phi + \frac{1}{Z_i e n_i}\boldsymbol{\nabla} P_i + \frac{5k_B}{2Z_i e}\boldsymbol{\nabla} T_i\right) + B_0\nabla_\parallel\left(\frac{V_{\parallel i}}{B_0}\right)\right] + \frac{2}{3n_i k_B}\nabla_\parallel(k_{\parallel i}\nabla_\parallel T_i) + \frac{2}{3n_i k_B}\boldsymbol{\nabla}_\perp(\kappa_{\perp i}\boldsymbol{\nabla}_\perp T_i) + \left(\frac{2m_e}{M_i}\right)\frac{T_e - T_i}{\tau_e} \quad \text{(App. Eq. 8)}$$

$$\frac{\partial T_e}{\partial t} = -\left(\frac{1}{B_0}\boldsymbol{b}\times\boldsymbol{\nabla}_\perp\phi + V_{\parallel e}b\right)\cdot\nabla T_e - \frac{2}{3}T_e\left[\frac{2n_e}{B_0}\boldsymbol{b}\times\boldsymbol{\kappa}\cdot\left(\boldsymbol{\nabla}_\perp\phi - \frac{1}{en_e}\boldsymbol{\nabla}P_e - \frac{5k_B}{2e}\boldsymbol{\nabla}T_e\right) + B_0\nabla_\parallel\left(\frac{V_{\parallel e}}{B_0}\right)\right] + 0.71\frac{2T_e}{3en_e}B_0\nabla_\parallel\left(\frac{J_\parallel}{B_0}\right) + \frac{2}{3n_ek_B}\eta_\parallel J_\parallel^2 + \frac{2}{3n_ek_B}\nabla_\parallel(k_{\parallel e}\nabla_\parallel T_e) + \frac{2}{3n_ek_B}\boldsymbol{\nabla}_\perp(\kappa_{\perp e}\boldsymbol{\nabla}_\perp T_e) - \left(\frac{2m_e}{M_i}\right)\frac{T_e-T_i}{\tau_e} \quad \text{(App. Eq. 9)}$$

$$\frac{\partial V_{\parallel i}}{\partial t} = -\left(\frac{1}{B_0}b\times\boldsymbol{\nabla}_\perp\phi + V_{\parallel i}b\right)\cdot\boldsymbol{\nabla}V_{\parallel i} - \frac{\nabla_\parallel(P_i+P_e)}{n_iM_i} \quad \text{(App. Eq. 10)}$$

$$\frac{\partial \varpi}{\partial t} = -\frac{1}{B_0}\boldsymbol{b}\times\boldsymbol{\nabla}_\perp\phi\cdot\nabla\varpi + B_0^2\nabla_\parallel\left(\frac{J_\parallel}{B_0}\right) + 2\boldsymbol{b}\times\boldsymbol{\kappa}\cdot\boldsymbol{\nabla}P + \mu_{i,\parallel}\nabla_{\parallel 0}^2\varpi \quad \text{(App. Eq. 11)}$$

$$\frac{\partial \psi}{\partial t} = \frac{1}{B_0}\nabla_\parallel\phi + \frac{\eta}{\mu_0}\boldsymbol{\nabla}_\perp^2\psi + \frac{\eta_H}{\mu_0}\boldsymbol{\nabla}_\perp^4\psi + \frac{1}{en_eB_0}\nabla_\parallel P_e + 0.71\frac{1}{eB_0}\nabla_\parallel T_e \quad \text{(App. Eq. 12)}$$

Similar, density n_i, ion/electron temperature T_i/T_e, ion parallel velocity $V_{\parallel i}$, vorticity ϖ and parallel magnetic vector potential are evolved. One thing should be noticed that, in our current turbulence model, we only evolve the perturbation part and treat the equilibrium (zero order) variables balanced and unchanged during this simulation, instead of evolving the total (equilibrium+fluctuation), which is different from the transport code. More details about BOUT++ turbulence model can be found in Ref. [15].

Deleted: in BOUT++ turbulence model, equilibrium and perturbation parts of each variable are separated and we only solve perturbed part, which is different from BOUT++ transport model. So the contribution of zero order drift effects are not taken into consideration in BOUT++ turbulence model. …

Formatted: Highlight

Acknowledgement

We would like to express our thanks to all the group members in BOUT++ team and CFETR physics team for their help on finishing this letter, and useful discussion with Dr. P. B. Snyder in General Atomics and Dr. J. R. Myra in Lodestar Research Corporation during 2018 BOUT++ workshop in Livermore. We also want to give the thanks to Dr. Sun Hee Kim in ITER Organization and Dr. L.L. LoDestro in Lawrence Livermore National Laboratory for providing the data of ITER 15MA Be/Ar steady state scenario. This work was performed under the auspices of the U.S. Department of Energy by Lawrence Livermore National Laboratory under Contract No. DE-AC52-07NA27344. This material is based upon the work supported by the U.S. Department of Energy, Office of Science, Office of Fusion Energy Sciences, and supported by under China Scholarship Council (CSC, under 201706010039), NSFC (Grant Nos. 41674165 and 11261140326) and National Magnetic Confinement Fusion Research Program of China (Grant No 2014GB107004). Numerical computations were performed on the National Energy Research Scientific Computing Center (NERSC), a U.S. Department of Energy Office of Science User Facility operated under Contract No. DE-AC02-05CH11231.

Reference:

[1] S. H. Kim et al. "Simulating Burning Plasma Operation in ITER," *paper ITER_D_R9T8J9 v1.1*, EPS, Lisbon, 2015

[2] Goldston R.J. 2012 *Nucl. Fusion* **52** 013009

[3] T. Eich et al 2013 *Nucl. Fusion* **53** 093031

[4] T. Eich, et al. *Phys. Review Lett.* **107**, 215001 (2011)

[5] Makowski M. *Phys. Plasmas* **19** 056122 (2012)

[6] Kukushkin A. et al 2013 *J. Nucl. Mater.* **438** S203

[7] A. Loarte et al., *J. Nucl. Mater.* **463** 401-405 (2015)

[8] J. R. Myra, *Phys. Plasmas* 22, 042516 (2015)

[9] C. S. Chang et al. *Nucl. Fusion* **57** 116023 (2017)

[10] B. D. Dudson, et al. *Comput. Phys. Commun.* **180** 1467 (2009)

[11] B. D. Dudson, et al, BOUT++, *Zenodo* https://doi.org/10.5281/zenodo.1423212

[12] Xu X.Q. et al. 2011 *Nucl. Fusion* **51** 103040

[13] Xu X.Q. et al. 2010 *Phys. Rev. Lett.* **105** 175005

[14] Xi P. W., Xu X. and Diamond P. *Phys. Rev. Lett.* **112** 085001(2014)

[15] T. Y. Xia, and X. Q. Xu, *Nucl. Fusion*, **55**, 113030 (2015)

[16] B. Chen, X.Q. Xu, et al. *Nucl. Fusion,* **57**, 116025 (2017)

[17] B. Chen, X. Q. Xu, et al. *Phys. Plasmas,* **25**, 055905 (2018)

[18] N.M. Li, et al. *Comp. Phys. Comm.* **228** (2018)

[19] B.D. Dudson, J. Leddy, *Plasma Phys. Control. Fusion* **59** 054010 (2017)

[20] B.D. Dudson et al., SD1D,https://github.com/boutproject/SD1D

[21] L. Easy, F. Militello et al., *Phys. Plasmas* **21**, 122515 (2014)

[22] N. M. Li, X. Q. Xu, et al., *In preparation*

[23] T. F. Tang et al. *Submitted to Phys. Plasma.*

[24] N. M. Li, et al. *Submitted to Nucl. Fusion.*

[25] P. F. Stangeby, *The Plasma Boundary of Magnetic Fusion Devices*, 2000

[26] T. D. Rognlien et al., *J. Nucl. Mater.* **363–365** (2007) 658–663

[27] D. Reiser and T. Eich, *Nucl. Fusion* **57** 046011 (2017)

[28] F. D. Halpern et al., *Phys. of Plasma.* **24**, 072502 (2017)

[29] B. Zhu et al. *Phys. of Plasma.* **24**, 055903 (2017)

[30] B. Zhu et al. *Comp. Phys. Comm.* **232** (2018)

[31] T. Casper et al., *Nucl. Fusion,* **54** (2014) 013005.

[32] A. C. Hindmarsh et al., *ACM Transactions on Mathematical Software*, **31(3)**, pp. 363-396, 2005.

[33] W Fundamenski, *Plasma Phys. Control. Fusion* **47** (2005) R163

[34] T. Eich et al., *J. Nucl. Mater.* **438** (2013) S72–S77

[35] X. Q. Xu, et al., 27th IAEA Fusion Energy Conference, Ahmedabad, India, Oct. 22-27, 2018